Weierstraß-Institut
für Angewandte Analysis und Stochastik

Leibniz-Institut im Forschungsverbund Berlin e. V.

Preprint ISSN 2198-5855

Modeling and simulation of the cascaded polarization-coupled system of broad-area semiconductor lasers

Mindaugas Radziunas[1], Volker Raab[2]

submitted: June 26, 2024

[1] Weierstrass Institute
Mohrenstraße 39
10117 Berlin
Germany
E-Mail: mindaugas.radziunas@wias-berlin.de

[2] Raab-Photonik GmbH
Amundsenstr. 10
14469 Potsdam
Germany
E-Mail: raab@optikexpertisen.com

No. 3116
Berlin 2024

2020 *Mathematics Subject Classification.* 78A60, 78A05, 65Z05, 78A55, 78-04.

Key words and phrases. Semiconductor laser, high-power, broad-area, edge-emitting, rectified polarization beam combining, scalability, Lyot filter, modeling, simulations.

This work was inspired by the EUROSTARS Project E!10524 HIP-Lasers.

Edited by
Weierstraß-Institut für Angewandte Analysis und Stochastik (WIAS)
Leibniz-Institut im Forschungsverbund Berlin e. V.
Mohrenstraße 39
10117 Berlin
Germany

Fax: +49 30 20372-303
E-Mail: preprint@wias-berlin.de
World Wide Web: http://www.wias-berlin.de/

Modeling and simulation of the cascaded polarization-coupled system of broad-area semiconductor lasers

Mindaugas Radziunas, Volker Raab

Abstract

We consider a brightness- and power-scalable rectified polarization beam combining scheme for high-power, broad-area edge-emitting semiconductor laser diodes. The coupling of 2^m emitters is achieved through Lyot-filtered optical reinjection from a specially designed multi-stage external cavity, which forces individual diodes to lase on interleaved frequency combs with overlapping envelopes. Simulations of up to sixteen coupled emitters and analysis of the calculated beams suggest that, under ideal conditions, a beam coupling efficiency of approximately 90% can be expected. Reducing optical losses within the external cavity is crucial for improving this efficiency in experimental systems.

1 Introduction

High-power broad-area edge-emitting semiconductor lasers (BALs) are key devices in many modern applications, often requiring over ten watts of emission power from a single diode and up to several kilowatts from a combined laser system [1]. Perfect power, brightness, and efficiency scaling of the combined lasers are strongly desired seeking to reduce the energy consumption and meet the demands of new applications. However, conventional beam-combining schemes have their limitations. For example, the side-by-side BAL coupling approach is power-scalable but lacks brightness scalability [2]. In contrast, spectral beam combining, achieved through various diffractive optical elements [3], increases combined beam power and brightness but suffers from optical spectrum broadening and can be affected by different thermal wavelength drifts of the individual emitters.

In this work, we explore a cascadable rectified polarization and spectral beam combining (RPBC) technique for coupling emitters with similar emission wavelengths, producing a combined output beam with a well-defined polarization state. The RPBC technique is both brightness- and power-scalable and preserves the width of the optical spectrum of the combined beam compared to the spectra of individual emitters [4]. Beam combining is achieved through Lyot-filtered optical reinjection from a shared external cavity (EC), which forces the individual diodes to lase on interleaved frequency combs with overlapping envelopes and should enable high optical coupling efficiency. 2^m emitters are coupled by the repeatedly introduced m stages of the specially designed EC, each specified by particular sets of optical elements; see Fig. 1 for a schematic representation of this system. Lyot filtering within this EC is realized by the proper positioning of polarization beam splitters and birefringent crystals of specially selected lengths [4, 5]. An experimental RPBC of 8 laser *bars* with a 64% optical coupling efficiency was discussed in [5]. To understand the reasons behind the suboptimal coupling efficiency, we model and simulate *individual* BAL emitters coupled with the RPBC scheme in this work. First, we briefly introduce a 2 (space)+1 (time)-dimensional traveling wave (TW) model [6] used to simulate the temporal-spatial dynamics in BALs, accounting for inhomogeneous current spreading [7] and heating [8] effects. Next, we present a detailed algorithm for constructing the multi-staged EC that induces

DOI 10.20347/WIAS.PREPRINT.3116 Berlin 2024

RPBC of 2^m emitters with arbitrary positive m. In particular, we present a method to determine the types of wave plates (depicted as small hatched boxes in Fig. 1) that should be positioned within all EC stages along the optical path from each individual emitter to the outcoupling mirror. Such an EC configuration is a nontrivial generalization of the single-stage cavity used for coupling two emitters and requiring a single half-wave plate in front of one of them [9]. Finally, we simulate the operation of two, four, eight, and sixteen coupled emitters, analyze the beam coupling efficiency, and discuss possible limiting factors of this coupling scheme. Deriving the algorithm for the location of the wave plates in the EC and demonstrating the coupling efficiency evolution with changes in the number of emitters and field losses in the EC stages are the main results presented in this work.

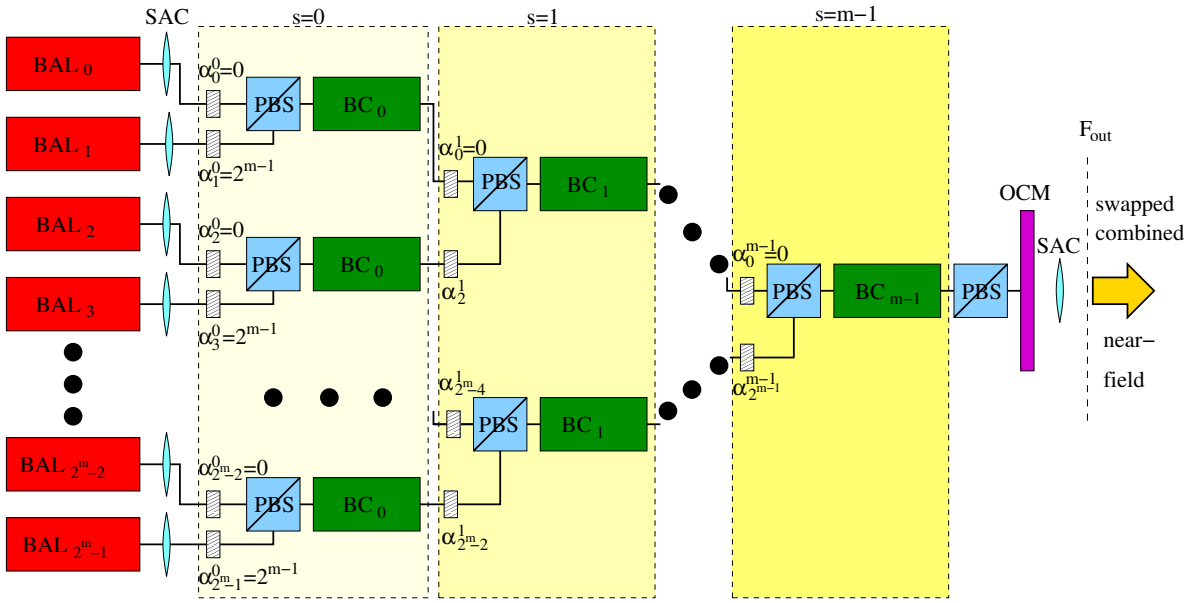

Figure 1: Schematic representation of the system of BALs coupled by the cascaded EC. Hatched small boxes: consequently located (α_l^s) $\lambda/2^m$-wave plates (or their equivalents). Light shadings: different stages of the EC.

2 Setup

We consider a system of 2^m BALs coupled via cascaded EC containing various optical elements such as slow-axis collimating (SAC) lenses, birefringent crystals (BCs), polarization beam splitters (PBSs), different wave plates (WPs), and a partially reflecting out-coupling mirror (OCM). A schematic representation of this system is shown in Fig. 1. To enable Lyot filtering, which is realized by the sequences of the PBS and BC in Fig. 1, the optic axis of the BC (calcite) must be inclined at 45° to the lateral (x) and vertical (y) directions. We note that this scheme ignores the vertical (fast axis) dimension, which in real-life setups should be handled by appropriately positioned fast-axis collimating lenses just behind the laser facets. In our modeling, we assume ideal fast-axis collimation. We also assume that the SAC lenses are perfectly perpendicular to the optical axes of each BAL and are located at their focal distance f from the laser facets. Another SAC lens outside the OCM transforms the k_x-space representations of the optical fields behind the close-to-facet lenses back to the standard space. The superposition of the emissions at the focal distance f behind the outer SAC lens (focal plane F_{out} in Fig. 1) forms a combined near-field of all BALs. The individual emissions are swapped with respect to

the corresponding optical axis, filtered on the way by Lyot filters (realized by combinations of PBS, BC, and another PBS), and undergo individual lateral-coordinate- and EC-length-dependent phase shifts.

The EC has m stages numbered by index $s = 0, \ldots, m-1$, each containing BCs of length $L_s = 2^s L_0$, PBSs, and WPs. There are 2^{m-1-s} BCs and PBSs and 2^{m-s} positions for different WPs within the s-th stage of the EC. The emission of each BAL passes through a single triple (WP, PBS, BC) within each stage on its way toward the OCM. Each WP-element (hatched boxes in 1) consists of an integer number α_l^s of sequentially located "elementary" $(\lambda/2^m)$-WPs, or only one or a few "larger" WPs, providing an equivalent change in the field polarization components. For example, $\alpha_l^s = 0$ indicates the absence of the WP at the expected position, while $\alpha_l^s = 2^{m-1}$ and 2^{m-2} of $(\lambda/2^m)$-WPs are equivalent to half- and quarter-wave plates, respectively. Any $\alpha_l^s \in \mathbb{Z}$ can be replaced by $(\alpha_l^s \mod 2^m)$.

To simplify the derivation of our algorithms, we write the indices of 2^m lasers or different paths towards the OCM in binary format,

$$j = \sum_{q=0}^{m-1} 2^q j_q = [j_{m-1}, \cdots, j_1, j_0],$$

where j_q is a q-th digit (0 or 1), indicating the absence or presence of 2^q within j. Digits j_q with $q < 0$ or $q \geq m$, if used, are set to 0. By setting the s lower-order binary digits of j to zero, we define "reduced" indices

$$\lfloor j \rfloor_s = \sum_{q=s}^{m-1} 2^q j_q = j - (j \mod 2^s).$$

For example, $\lfloor j \rfloor_0 = j$, $\lfloor 0 \rfloor_s = 0$, and $\lfloor j \rfloor_{m-1} = 2^{m-1} j_{m-1}$. According to the construction of the setup, see Fig. 1, each WP-element denoted by $\alpha^s_{\lfloor j \rfloor_s}$ within stage s is bypassed by emissions of 2^s BALs with a common reduced index $\lfloor j \rfloor_s$.

In what follows, we assume there are no wave plates on the path from BAL_0 to the OCM, i.e., $\alpha_0^s = 0$ for $s = 0, \ldots, m-1$. The ideal PBSs in stage 0 fully transmit x-polarized light and absorb y-polarized light from BALs with even indices j, and vice versa for BALs with odd indices. Since we assume x-polarized emission from all BALs, we set $\alpha_j^0 = j_0 2^{m-1}$. This means no WPs are in front of BALs with even indices (their x-polarized light directly enters the PBSs), while $(\lambda/2)$-WPs are placed in front of BALs with odd indices to switch x- and y-polarizations (so y-polarized light enters the PBSs). The remaining integers α_l^s are defined in the algorithm discussed in Section 4.

3 Mathematical model

To model the nonlinear dynamics in BALs, we employ a (2+1)-dimensional TW model [6] and the electro-optical (EO)-solver BALaser [10]. This model is based on TW equations describing the slowly varying complex amplitudes of the counter-propagating TE-polarized fields $E_j^{\pm}(z, x, t)$ within the active zone of each BAL_j:

$$\left[\tfrac{n_g}{c_0}\partial_t \pm \partial_z + \tfrac{i}{2\bar{n}k_0}\partial_x^2\right] E_j^{\pm} = -i\beta(N_j, E_j^{\pm}, \theta_j) E_j^{\pm} + F_{sp}^{\pm}. \tag{1}$$

Here c_0, n_g, $\bar{n}$, and $F_{sp}^{\pm}$ are the speed of light in vacuum, the group velocity index, the reference refractive index, and the Langevin noise, respectively. $k_0 = 2\pi/\lambda_0 = \omega_0/c_0$ is the free-space central wavenumber, with λ_0 and ω_0 denoting the central wavelength and frequency, respectively. The complex factor β accounts for absorption, induced refractive index profile, material gain, and refractive index. The latter two factors rely on the carrier density $N_j(z, x, t)$, capturing nonlinear gain compression and material gain dispersion. The diffusive (in x) rate equation governs the dynamics of N [6].

Carrier diffusion and injected current are determined by simultaneously solving the current spreading problem in lateral/vertical (x/y) cross-sections of the BALs [7], with the bias voltage at the electrical contact serving as the driving parameter of the entire EO model. Additionally, we alternate $\sim 5\,\mathrm{ns}$ transient simulations of the EO model with the solution of the static heat-flow model. This provides insights into the three-dimensional time-averaged temperature distribution in the diodes, the temperature $\theta_j(x,z)$ at the active zone, and the heating-induced corrections to the refractive index and some other model parameters [8].

At the lateral borders of the (sufficiently broad) computational domain, which significantly exceeds the width of the contact stripe, w_c, periodic conditions are imposed on $E_j^{\pm}$ and N_j. At the high-reflecting rear facets, $z=-l$, reflecting conditions $E_j^+(-l,x,t) = \sqrt{R_r}E_j^-(-l,x,t)$ are enforced. Finally, at the low-reflecting front facet ($z=0$), facing the EC, another reflecting condition is applied, with additional reinjection from the EC:

$$\begin{aligned} E_j^-(0,x,t) &= \sqrt{R_f}E_j^+(0,x,t) + \sqrt{T_f}E_j^r(x,t),\\ E_j^r(x,t) &= \textstyle\sum_{r=0}^{2^m-1}[M_{[j,r]}E_r^e](x,t). \end{aligned} \tag{2}$$

$R_r \lesssim 1$, $R_f \ll 1$, and $T_f = 1-R_f$ are field intensity reflections and transmission at the corresponding facet. E_j^r and $E_j^e(x,t) = \sqrt{T_f}E_j^+(0,x,t)$ represent the reinjected and emitted x-polarized fields just outside the front facet of BAL$_j$. The combined beam at the F_{out} plane behind the OCM (see Fig. 1) is given by

$$E^c(x,t) = \textstyle\sum_{r=0}^{2^m-1} E_r^c(x,t), \quad E_r^c = [M_{[r]}E_r^e](x,t). \tag{3}$$

The scalar operators $M_{[j,r]}$ and $M_{[r]}$ in (2) and (3) are the upper left elements of 2×2-dimensional matrix operators $\mathbf{M}_{[j,r]}$ and $\mathbf{M}_{[r]}$, respectively. These matrices translate the (x- and y- polarized) vector-field $\mathbf{E} = (E_x, E_y)^T$, where T denotes transposition, from BAL$_r$ to BAL$_j$ or to the F_{out} plane. Both vector field components interchange within BCs and WPs. The matrix propagators are sequential superpositions of "elementary" matrix operators (see Appendix and [9]), each defining the field propagation within different optical elements of the EC. For constructing efficient models, we employ a paraxial approximation of the wave equations, neglecting differences in optical path lengths and backscattering from all (antireflection coated) elements of the EC. We use an idealized thin lens model, assume perfect polarization splitting in PBSs, and exploit the commutativity of different elementary operators. The configuration of the EC implies that all but the upper-left components of $\mathbf{M}_{[j,r]}$ and $\mathbf{M}_{[r]}$ vanish, such that optical feedback and combined beams are x-polarized. Consequently, the resulting local in time and space operators $M_{[j,r]}$ and $M_{[r]}$ are sums of several telescope-type operators,

$$\begin{aligned} M_{f,\delta}^{\mathrm{tel}} &= M_f^{\mathrm{pr}} M_f^{\mathrm{ln}} M_{2f+\delta}^{\mathrm{pr}} M_f^{\mathrm{ln}} M_f^{\mathrm{pr}}\\ &= ie^{i(2\phi_{\mathrm{ln}}-4fk_0)} e^{i\delta k_0(\frac{x^2}{2f^2}-1)} M^{\mathrm{sw}} M_{(4f+\delta)/c_0}^{\mathrm{sh}}. \end{aligned} \tag{4}$$

Here, M_d^{pr} is a free-space propagator over the distance d, M_f^{ln} models transmission through a thin lense with f and ϕ_{ln} denoting the focal distance and the lens-induced fixed phase shift, M^{sw} is a coordinate-swap, and M_τ^{sh} defines a time delay, see Appendix and [9] for more details. The operator $M_{[j,r]}$ for two coupled diodes was also defined in [9]. For arbitrary m,

$$\begin{aligned} M_{[r]} &= \tfrac{\sqrt{\kappa T_e}}{2^m} \sum_{k'=0}^{2^m-1} \eta_r^{k'} M_{f,d_{k'}+l_r-3f}^{\mathrm{tel}} M_{\rho_{k'}}^{\mathrm{sh}},\\ M_{[j,r]} &= \tfrac{\kappa\sqrt{R_e}}{4^m} \sum_{l',k'=0}^{2^m-1} \eta_j^{l'} \eta_r^{k'} M_{f,d_{l'}+d_{k'}+l_j+l_r-4f}^{\mathrm{tel}} M_{\rho_{l'}+\rho_{k'}}^{\mathrm{sh}},\\ \eta_r^{k'} &= e^{i2\pi \sum_{s=0}^{m-1} \left(\left(\frac{\alpha_{\lfloor r\rfloor_{s+1}}^{s+1}}{2^m} - \frac{r_s+r_{s+1}}{2} \right) k'_s - \frac{n'_0}{\Delta'} \frac{\alpha_{\lfloor r\rfloor_s}^{s}}{2^m} \right)} e^{ik_0(d_{k'}-\nu_{k'})}. \end{aligned}$$

Here, l_j is the length of all air gaps between BAL$_j$ and the OCM, $\xi_{l'} = \sum_{s=0}^{m-1} \xi_{l'_s}$ are cumulative sums of the related coefficients within all coupling stages, where l'_s is s-th digit of the binary representation of l', while

$$\tau_{l'_s} = \frac{L_s n''_{l'_s}}{c_0},\ d_{l'_s} = \frac{L_s}{n'_{l'_s}},\ \nu_{l'_s} = L_s n'_{l'_s},\ \rho_{l'_s} = \tau_{l'_s} - \frac{d_{l'_s}}{c_0}. \tag{5}$$

n'_ι and n''_ι are the refractive and group indices along the ordinary ($\iota = 0$) and extraordinary ($\iota = 1$) axes of the BCs, whereas $\Delta' = n'_0 - n'_1$ and $\Delta'' = n''_0 - n''_1$ are the birefringence parameters. R_e and $T_e = 1 - R_e$ are intensity reflection and transmission at the OCM, while $\kappa = (1-\mu)^m$, with μ denoting lumped field intensity losses per coupling stage, is the correction factor of the field transmission through the entire EC. In the case of the "ideal" EC ($\mu = 0$), $\kappa = 1$. Due to Eq. (4), the operator $M_{[j,r]}$ entering boundary conditions (2) is given by

$$\begin{aligned}
&M_{[j,r]} = \tfrac{i\kappa\sqrt{R_e}}{4^m} M^{\mathrm{sw}} \sum_{l',k'=0}^{2^m-1} \chi_j^{l'} \chi_r^{k'} M^{\mathrm{sh}}_{\tau_{l'}+\tau_{k'}+(l_j+l_r)/c_0},\\
&\chi_j^{l'} = e^{i(\phi^x_{j,l'} x^2 + \phi_{j,l'} + \phi^\alpha_{j,l'})},\\
&\phi^x_{j,l'} = \tfrac{k_0(d_{l'}+l_j-2f)}{2f^2},\ \ \phi_{j,l'} = \phi_{\ln} - k_0(\nu_{l'} + l_j),\\
&\phi^\alpha_{j,l'} = 2\pi \sum_{s=0}^{m-1} \Big(\Big(\tfrac{\alpha^{s+1}_{\lfloor j \rfloor_{s+1}}}{2^m} - \tfrac{j_s + j_{s+1}}{2} \Big) l'_s - \tfrac{\alpha^s_{\lfloor j \rfloor_s}}{2^m} \tfrac{n'_0}{\Delta'} \Big).
\end{aligned} \tag{6}$$

For further details on the modeling of elementary operators and construction of overall propagators, see Appendix and [9].

4 Algorithm for the wave plate selection

Until now, we have not determined the WP parameters $\alpha^s_{\lfloor j \rfloor_s}$, which are crucial for achieving correctly interleaving spectral combs of different BALs and avoiding unnecessary field losses within the EC. Let us assume $\kappa = 1$ and search for a configuration that allows different wavelength-shifted self-reflections of all BALs, with the peak self-reflection intensity R_e. We shall assume that all lasers radiate the same plane wave (only the x-polarization component) given by $E = e^{i(\bar{k}x + \omega t)}$. Feedback operators applied to this plane wave for different frequencies ω define complex reflectivity spectra

$$\mathcal{R}_{j,r}(\omega, x) = \tfrac{M_{[j,r]} E(x,t)}{E(x,t)} = e^{-i(\bar{k}x+\omega t)} M_{[j,r]} e^{i(\bar{k}x+\omega t)}.$$

The self-feedback at $x = 0$,

$$\mathcal{R}_{j,j}(\omega, 0) = \tfrac{i\sqrt{R_e}}{4^m} \sum_{l',k'=0}^{2^m-1} \chi_j^{l'} \chi_j^{k'} e^{-i\omega(\tau_{l'}+\tau_{k'}+\frac{2l_j}{c_0})},$$

is a sum of 4^m harmonic oscillators. Its intensity

$$|\mathcal{R}_{j,j}|^2 = \tfrac{R_e}{16^m} \Big| \sum_{l',k'=0}^{2^m-1} e^{i(\phi^\alpha_{j,l'} + \phi^\alpha_{j,k'} - k_0(\nu_{l'}+\nu_{k'}) - \omega(\tau_{l'}+\tau_{k'}))} \Big|^2$$

can reach the maximal possible value of R_e at certain frequencies ω^*_j where all summed exponents determined by indices l' and k' satisfy (by modulus 2π) an equal phase condition (EPC)

$$\phi^\alpha_{j,l'} + \phi^\alpha_{j,k'} - k_0(\nu_{l'} + \nu_{k'}) - \omega^*_j(\tau_{l'} + \tau_{k'}) = \bar{\varphi}_j. \tag{7}$$

For each j, EPC (7) is a system of 4^m equations corresponding to different pairs of indices (l', k'). Since almost all notations in this system are parameters of the EC, most of which are defined in Eqs. (5) and (6), it can be interpreted as an overdetermined liner system with respect to the unknown phase $\bar{\varphi}_j$ and frequency ω_j^*. By eliminating the phase $\bar{\varphi}_j$ from this system (using Eq. (7) for $l' = k' = 0$, for example) and exploiting all above-introduced definitions of the EC parameters, we can show that EPC (7) can be fulfilled if only

$$\frac{\alpha^{s+1}_{\lfloor j \rfloor_{s+1}}}{2^m} - \frac{j_s + j_{s+1}}{2} + \frac{2^s L_0}{\lambda_0}\left(\Delta' + \frac{\Delta'' \omega_j^*}{\omega_0}\right) \in \mathbb{Z}, \;\; 0 \le s < m.$$

Next, let us assume that the optimal ω_j^* reappears with the (smallest) period T_ω^j. This assumption, valid for all $s \ge 0$, gives us the condition $T_\omega^j = \frac{2\pi c_0}{L_0 \Delta''}$, which is the same for all BALs, i.e., $T_\omega^j = T_\omega$. Due to our assumption of $\alpha_0^s = 0$ (no WPs on the way of BAL$_0$), we can fix $\omega_0^* = Z_0 T_\omega - \frac{\omega_0 \Delta'}{\Delta''}$, where Z_0 is an integer which shifts ω_0^* to the domain of interest. The remaining optimal positions ω_j^* have to be located at $\omega_0^* + \nu_j T_\omega$, where $\nu_j \in [0, 1)$. The EPC can be rewritten as

$$2^s \nu_j + \frac{\alpha^{s+1}_{\lfloor j \rfloor_{s+1}}}{2^m} - \frac{j_s + j_{s+1}}{2} \in \mathbb{Z}, \quad s = 0, \dots, m-1. \tag{8}$$

In the optimal case of correctly interleaved spectral combs, the shift factors are given by $\nu_j = 2^{-m} j'(j)$, where j' is an invertible integer function of j with values belonging to $[0, 2^m)$. In our algorithm we define the integer function j' as the binary conjugate of j. This means that its binary representation $[j'_{m-1}, \dots, j'_1, j'_0]$ coincides with the reversed binary representation of j, such that $j'_q = j_{m-1-q}$. Therefore,

$$j'(j) = \textstyle\sum_{q=0}^{m-1} 2^q j'_q = \sum_{q=0}^{m-1} 2^{m-1-q} j_q. \tag{9}$$

Obviously, there is a unique one-to-one correspondence between j and j'. Now, we substitute $\nu_j = \frac{j'(j)}{2^m}$ using j' from Eq. (9) into EPC (8). By setting the resulting expressions to zero, we obtain the required integer $\alpha^s_{\lfloor j \rfloor_s}$ (modulus 2^m) defining all the remaining WPs within the coupling stages for $s = 1, \dots, m-1$:

$$\alpha^s_{\lfloor j \rfloor_s} = 2^{m-2}\big[j_s - \sum_{q=s+1}^{m-1} 2^{s-q} j_q\big] \mod 2^m. \tag{10}$$

Once the WPs are located according to (10), the field intensity transmission and self-reflection spectra at $x = 0$ are given by

$$\begin{aligned} |\mathcal{T}_j(\omega, 0)|^2 &= \tfrac{T_e}{4^m}\Big|\textstyle\sum_{l'=0}^{2^m-1} e^{i\frac{2\pi l'}{T_\omega}(\omega - \omega_j^*)}\Big|^2, \\ |\mathcal{R}_{j,j}(\omega, 0)|^2 &= \tfrac{R_e}{T_e^2}|\mathcal{T}_j(\omega, 0)|^4. \end{aligned} \tag{11}$$

Being defined by the sum of several exponents, frequency-domain functions $|\mathcal{T}_j(\omega, 0)|^2$ and $|\mathcal{R}_{j,j}(\omega, 0)|$ resemble the time-trace of the mode-locked pulsations.

An example of perfectly interleaving self-reflection spectra of eight BALs (case of $m = 3$) at $x = 0$ is shown in Fig. 2(a). Panel (b) shows the intensities of the self-reflection $\mathcal{R}_{0,0}$ and all cross-reflections $\mathcal{R}_{j,0}$ from BAL$_0$ to BAL$_j$ around the optimal ω_0^* for the same 8-diode case. One can see that the cross-reflections of the emission with $\omega = \omega_0^*$ vanish, while the self reflection at the same frequency is maximal. For frequencies deviating from ω_0^*, the self-feedback decreases, while the cross-feedback intensity can reach about 16%. Finally, panel (c) of the same figure represent the scaled $|\mathcal{R}_{0,0}|^2$, transmission $|\mathcal{T}_0|^2$ (which coincides with the total field intensity $\sum_{r=0}^{m-1} |\mathcal{R}_{r,0}|^2$ returning to *all* diodes from BAL$_0$), and the losses of the BAL$_0$ emission intensity within the EC, $1 - |\mathcal{T}_0|^2$, near ω_0^*. Here, one

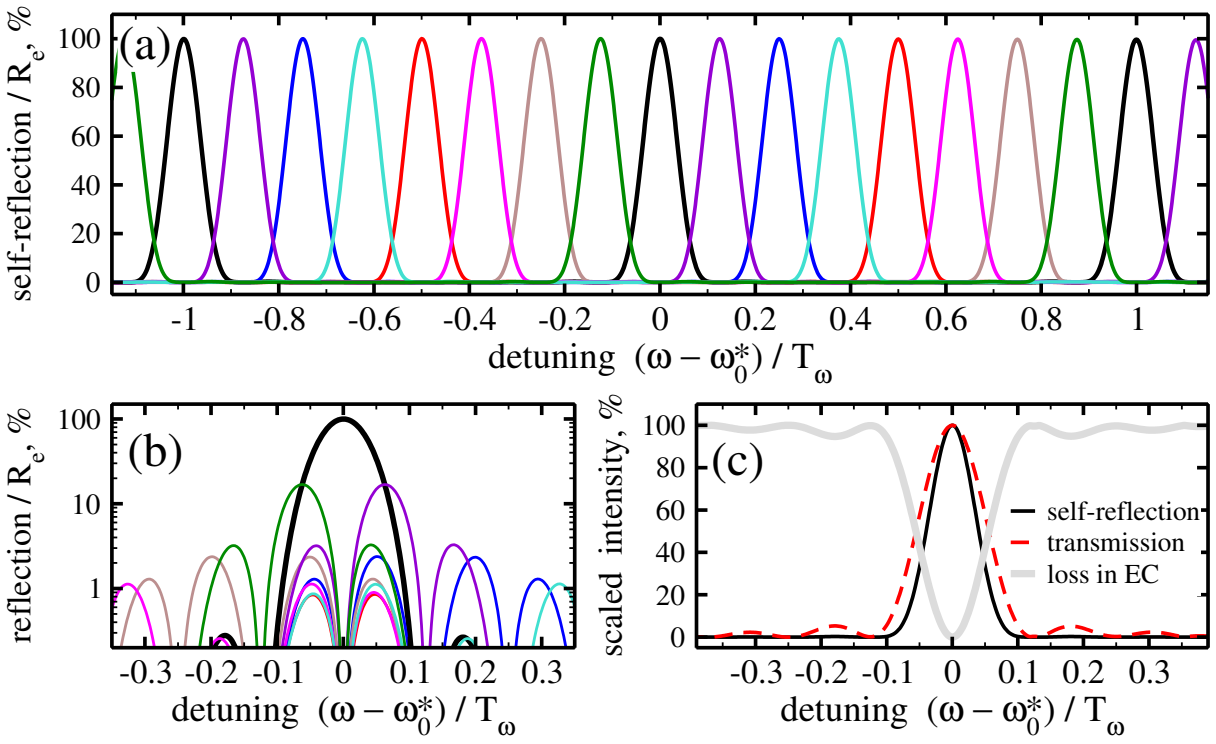

Figure 2: Spectral properties of the 3-staged EC. (a): Self-reflections of all 8 diodes. (b): Self- (thick) and cross-reflections (thin) of BAL_0 in the vicinity of ω_0^*. (c): Scaled self-reflection (solid black), transmission (dashed) and loss spectra of BAL_0 near ω_0^*.

can see that with increasing detuning from the optimal ω_0^*, the losses rapidly increase. Thus, the high coupling efficiency of the coupled diodes can only be achieved when Lyot-filtered feedback forces the diodes to operate as close to their optimal T_ω-periodically reappearing frequencies ω_j^* as possible.

Summarizing the discussion above, we note the following. In the ideal case, the feedback provided by the EC to each BAL_j enhances the laser modes whose frequencies are located at the peak filtering positions ω_j^*. These modes dominate over all other (suppressed) modes. Each BAL, in this case, receives the maximum possible self-feedback without cross-talk with neighboring BALs. With perfect (lossless) optical components, optical losses within the EC are absent, leading to a beam coupling efficiency close to 1. In a more realistic (yet still optimal) case, the BALs will operate within nonvanishing frequency ranges around ω_j^*. This occurs because the positions of ω_j^* are "smeared" and depend on the transverse coordinate x: $\omega_j^*(x) = \omega_j^*(0) - \frac{\omega_0 \Delta'}{2 n_0' n_1' \Delta'' f^2} x^2$. Besides, this smearing is implied by the discreteness of the main mode frequencies and the diodes' resistance to the mode filtering by optical feedback.

Consequently, self-feedback will be suboptimal, with its relative intensity being less than R_e. Part of the emission will be redirected to neighboring BALs, and some will be lost at the PBSs of the EC. With this understanding, we will now proceed to a full simulation of the polarization-coupled BAL system to further analyze the coupling efficiency and feedback dynamics under realistic conditions.

5 Simulations

We have simulated several configurations of coupled BALs characterized by the same parameters and operated at identical bias voltages. The current-spreading model was used, meaning that the same voltage could result slight differences in the total bias current per emitter. In all cases, the diodes were 4 mm long, had 95% rear-facet reflectivity R_r and 1% front-facet reflectivity R_f, operated around $\lambda_0 = 970$ nm, and emitted approximately 12 W. The setup included $5\,\mu$m trenches with a 0.004 refractive index step, positioned $5\,\mu$m aside of $w_c = 100\,\mu$m (or, in some examples, $200\,\mu$m) broad contacts. Within the EC, we considered SAC lenses with $f = 2$ cm, BCs (calcite) with lengths $L_s = 2^s \cdot 4$ mm in the s-th stage of the EC, and equal total air-gap lengths $l_j = 20$ cm (including optical path lengths of the lenses, WPs, and PBSs). Unless specified otherwise, the setup had 4% OCM reflectivity R_e and vanishing lumped losses μ. These ECs induced different delays, ranging from about 1.4 ns for a single-stage EC to about 2 ns for a four-stage EC. The periodicity of the Lyot filters is around $T_\omega \approx 2.64$ rad/ps in the frequency domain, which corresponds to approximately ~ 1.32 nm in the wavelength domain, as illustrated in Figs. 3(a). For more details on the laser and EC parameters, as well as the operation of two coupled emitters (in the case of $m = 1$), see [9]. In this study, we explore laser configurations with up to four coupling stages ($m \leq 4$).

Simulated optical spectrum, near- and far-fields of a solitary laser with a $100\,\mu$m-broad contact and no optical feedback are presented in the upper panels of Fig. 3. The lower panels of the same figure depict individual interleaving optical spectra (a), angular (b), and lateral (c) distributions of the fields at the front facets of the diodes, along with scaled combined beams of 2/4/8/16 emitters. The interleaved spectra in panels (a) demonstrate the efficient diode-mode selection achieved by the Lyot-filtered optical feedback. A closer examination of these spectra reveals small but nonvanishing contributions at wavelengths typical for the peak filtering positions of the neighboring lasers. This indirectly confirms the diode coupling since part of these contributions is reinjected into the neighboring emitters. The coupling scheme induces some broadening of the combined beam's spectral, spatial, and angular characteristics compared to those of the single BAL. For a better comparison of these characteristics in a single BAL and different combined BAL setups, we calculated the spectral, angular, and lateral ranges containing 95% of the solitary laser emission or combined beam power; see the light shading ranges in all diagrams of Fig. 3. After a noticeable increase in the spectral and angular beam widths when switching from the solitary BAL to the system of two coupled lasers, cf. light shading of the upper and second rows in Fig. 3(a) and (b), these widths remain almost constant with further extension of the combined system. The estimated angular (W_θ) and lateral ($W_x \approx w_c$) widths of the combined beam define a beam parameter product (BPP) of this beam along the slow axis, $\mathrm{BPP} = W_\theta W_x/4$.

Besides maintaining spectral and spatial characteristics of the combined beams similar to those of the solitary laser, we aim for the (time-averaged) power $P_c^{(m)}$ behind the OCM to remain comparable to the combined power $P_f^{(m)}$ of all 2^m emitters at their front facets, as well as to the power of the solitary emitter, $P_f^{(0)}$, multiplied by 2^m. To estimate these relations, we introduce the coupling efficiency factor representing the part of the field intensity transmitted through the EC and OCM: $\eta = P_c^{(m)}/P_f^{(m)} = \kappa T_e(1 - A_f)$, where A_f represents the part of the field intensity lost at the PBSs due to deviation of lasing modes of each BAL$_j$ from the optimal frequencies ω_j^*. Such losses in the frequency domain are represented by the thick light grey curve in Fig. 2(c).

Figure 4 illustrates the variations in different characteristics of 8 coupled emitters, each operating at approximately 12 W, with an increase in the OCM reflectivity R_e. Here, we represent three ns-time averages of calculated individual and combined emissions. For $R_e \gtrsim 2$%, the combined field intensity behind the OCM remains nearly constant (solid line in panel (a)), whereas the total emission

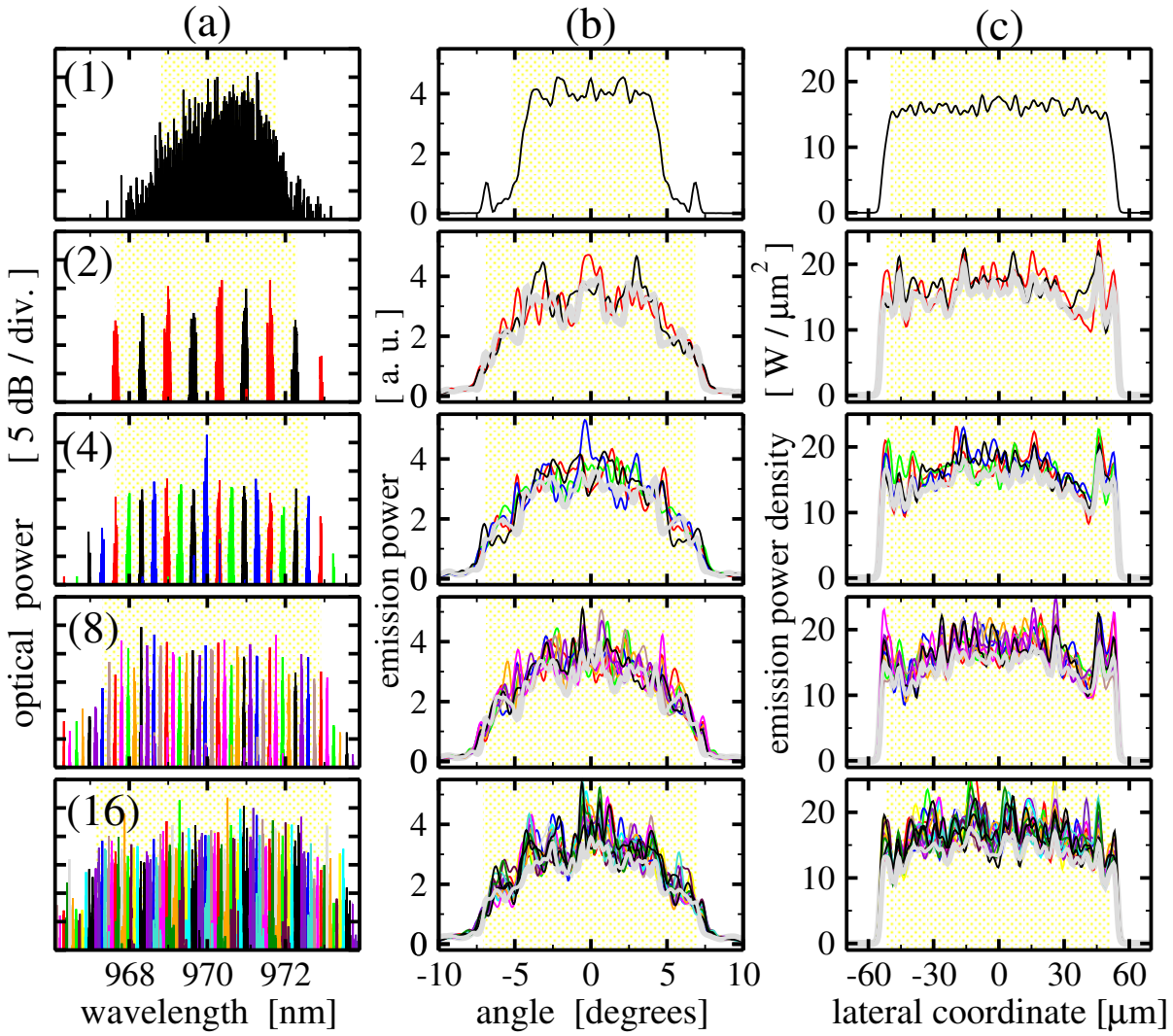

Figure 3: Simulations of a single diode without feedback (1) and 2/4/8/16 coupled diodes (corresponding lower rows). Optical spectra (a), far fields (b), and intensities (c) estimated for individual diode emissions at the front facet (thin lines). Thick gray curves in (b) and (c) and light shading in all panels represent the combined beam divided by the number of emitters at the F_{out} plane and regions containing 95% power content of these beams.

at the facets slightly increases (dashed line), as is implied by the growing amount of feedback into the diodes. The portion of the field that can be transmitted through the EC remains relatively unchanged (dashed line in panel (b)). However, the beam combining efficiency η gradually decreases with the increasing OCM reflection R_e (i.e., decreasing transmission T_e). The EC transmission reaching about 92% indicates that each BAL$_j$ emits at frequencies close to the optimal ω_j^* (by modulus T_ω), as seen in panels (a) of Fig. 3. This mode selection is induced by the Lyot-filtered feedback. We note that an increase in the feedback (or an increase of R_e) alone can not further improve the mode selection, and about 8% of the emission intensity is lost at the PBSs within the otherwise ideal EC. As R_e decreases and the amount of feedback reduces, the mode filtering becomes less pronounced, leading to a decline in the transmission $1 - A_f$, coupling efficiency η, and the combined beam power $P_c^{(3)}$ behind the OCM. Hence, to achieve the best possible mode filtering and beam combining, it's crucial to choose the OCM with $R_e \gtrsim (2/\kappa^2)\%$.

The increase in optical feedback, however, can also have a negative impact on the quality of the

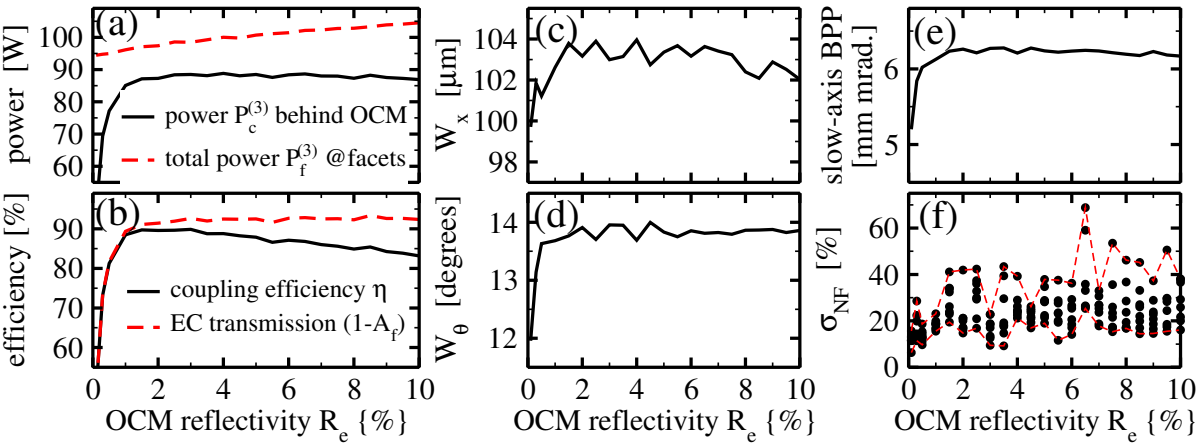

Figure 4: Simulated time-averaged emission of 8 coupled BALs for different OCM reflections R_e. (a): Total power at the front facets (dashed) and behind the OCM (solid). (b): Beam combining efficiency (solid) and field intensity transmission through the EC (dashed). (c) and (d): Lateral and angular width (95% of power content) of the combined beams. (e): Corresponding slow-axis BPP of these beams. (f): Largest near-field peaks at the facets of each emitter (dots) compared to over the contact width averaged field intensity. Thin dashed: largest and smallest of these maxima.

individual BAL emission. Panels (c)-(e) of Fig. 4 show the lateral and angular widths and the slow-axis BPP of the combined beam at the F_{out} plane behind the OCM. In the solitary BAL operated at the same bias, these factors were $100.37\,\mu$m, $10.4\,^\circ$, and 4.55 mm·mrad, respectively. Thus, an introduced feedback induces a visible broadening of the angular spectra and about a 30% increase of the BPP. Moreover, optical feedback also implies an enhancement of the (time-averaged) filaments, which results in a pronounced fluctuation of an otherwise pretty flat near field profile at the front facet of the diode, cf. upper and four lower diagrams of Fig. 3(c). To compare the peak power of these filaments and the averaged power density across the contact stripe in each BAL$_j$, we estimate the factor

$$\sigma_{NF}^{(j)} = \left[\max_x \langle |E_j^e(x,t)|^2\rangle_t \big/ \left(\tfrac{1}{w_c}\int \langle |E_j^e(x,t)|^2\rangle_t dx\right)\right] - 1,$$

with $\langle A\rangle_t$ denoting temporal averaging. Fig. 4(f) shows that the peak power can easily exceed the averaged near-field densities by 40% and can lead to the damages of the facet coating [11] of one or several emitters in the coupled-BAL setup. The factor σ_{NF} for the solitary BAL was about 6%.

Simulations of 8 coupled emitters with $200,\mu$m-wide contacts, each operating at the same 12 W, reveal more dramatic changes. The simulated efficiencies η of this setup were comparable to those of the above-discussed case. Due to the halved power density at the facets, up to $80\,$% intensity fluctuations were observed, which will likely still be harmless for the facet coating. However, the BPP of the combined beam increases from 7.07 (case of the solitary emitter) to about 13.5 mm·mrad (case of 2/4/8/16 coupled diodes with $R_e = 4\,$%). The main reason for this change is the broadening of the angular emission of individual diodes from $8.3°$ to about $15.6°$. A deeper analysis of feedback-induced large near-field intensity fluctuations and broadening of the far fields is a subject for further investigations.

In previous figures, we demonstrated beam combining implied by the ideal EC with the transmission prefactor $\kappa = 1$ (or vanishing losses μ). Fig. 5 represents the coupling of about $12\,$W emitting diodes for gradually increased loss factor μ. Note that in contrast to the left column diagrams, the right column panels show the operation of less saturated BALs, which have doubled contact stripe width and, therefore, halved photon density. Top and middle-row panels of Fig. 5 show the expected decaying

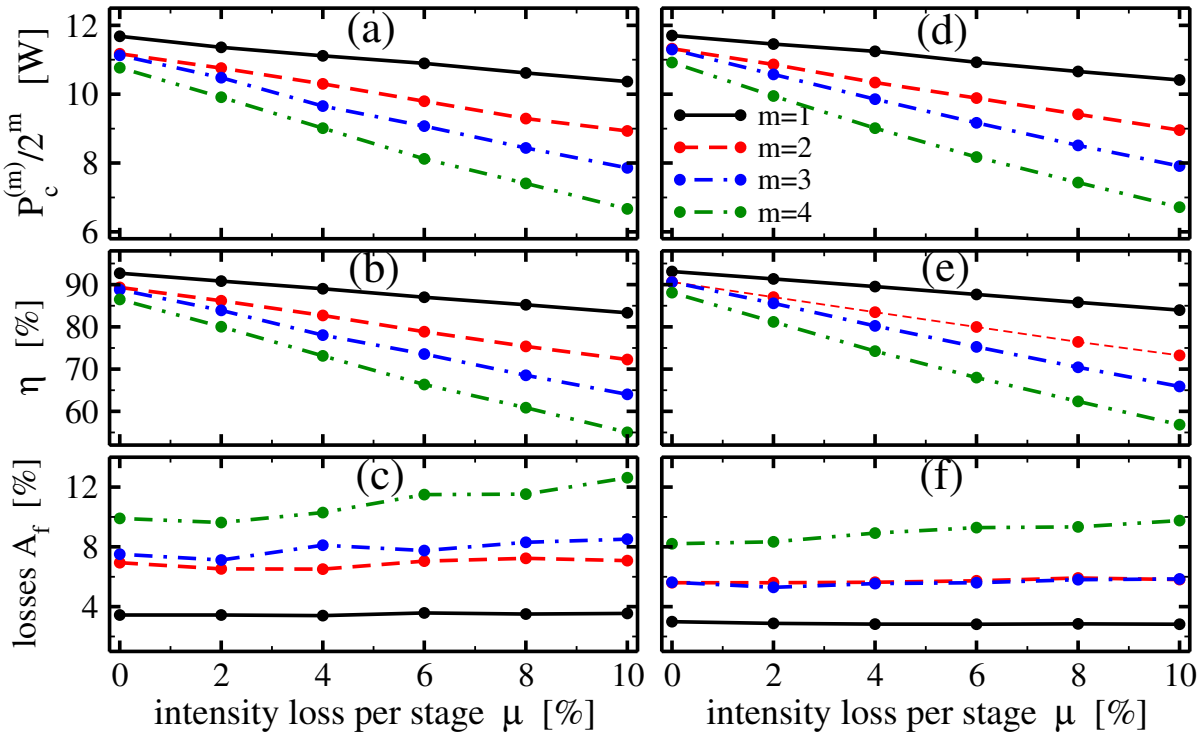

Figure 5: Simulated beam combining of 2/4/8/16 coupled diodes with $w_c = 100\,\mu$m (left) and $w_c = 200\,\mu$m (right) for different coupling stage loss rates μ. (a,d): Total time-averaged power behind the OCM scaled by the number of emitters. (b,e): Coupling efficiency. (c,f): Losses within the EC induced by the non-ideal filtering of the diode modes.

intensity of the combined field and the coupling efficiency with an increasing loss factor μ. Moreover, this decay is close to linear, which is because of the nearly constant contribution of the filtering-induced losses A_f for each considered coupled-laser configuration; see lower panels of Fig. 5. The value of A_f grows with the additional coupling stages, which is related to the narrowing of the filtering frequency bands of the multi-staged Lyot filters. It is interesting to note that these losses for 2- and 3-staged coupled laser configurations are similar; see dashed and dash-dotted lines in Fig. 5(c) and (f). A slight growth of A_f for the 4-staged configuration (dash-double dotted line) is due to reduced Lyot-filter-induced mode selection in the BALs, related to the decreasing maximal reinjection ratio, which drops to $R_e\kappa^2 \approx 1.7\,\%$ for $\mu = 10\%$ and $R_e = 4\%$ used in the considered case. The observed average growth of A_f with the number of stages does not exceed 4%, which allows us to expect a pretty good performance of the further combined BAL systems provided the loss factor μ is minimized, i.e., all optical elements, their anti-reflection coatings, and their positioning within the EC are close-to-perfect.

6 Conclusions

This work presents an algorithm for constructing a cascaded coupling scheme of 2^m emitters with arbitrary integer number m of coupling stages. This scheme aims to fulfill several key properties. Firstly, it ensures that the self-reflection peak wavelengths λ_j^* of all emitters reappear periodically with a period T_λ, which is inversely proportional to the length of the BC within the EC stage 0. Secondly, it ensures that the self-reflections of all emitters are spectrally interleaved, with λ_j^* and λ_l^* for any two emitters separated by $\frac{kT_\lambda}{2^m} \bmod(T_\lambda)$, where k is some integer from $\{1, \ldots, 2^m - 1\}$. Finally, the

algorithm aims to maximize the self-reflection intensity for each emitter at λ_j^*. The critical factor for achieving such a configuration is the proper choice and placement of wave plates within all stages of the EC along the optical path between each individual emitter and the outcoupling mirror. Eq. (10) provides the rule for determining the number of $(\lambda/2^m)$-WPs required at each such position.

Simulations of coupled BAL systems with up to four coupling stages have demonstrated that such ECs can act as efficient wavelength filters for each BAL, and the power of the combined beam is almost 2^m times larger than that of a solitary BAL. In contrast, other properties of the combined beam, such as spectral or far- and near-field widths, remain comparable to those of a solitary laser. It is important to note that these simulations were performed assuming nearly perfect optical elements and their precise placement within the EC. For an ideal EC, the beam coupling efficiency η for two coupled emitters was about 92%, decreasing by approximately 2% with each additional coupling stage. This reduction is primarily due to the diminishing impact of the Lyot-filtered feedback on the internal modes of the diodes. Extending the filters by an additional stage results in halving the individual wavelength-filtering bands, which diminishes self-feedback for modes with sub-optimal wavelengths and increases cross-talk between different coupled emitters whose filtering bands are now twice as close to each other. The coupling efficiency calculated in this work for idealized EC is significantly higher than the $\leq$80% reported for two coupled laser bars in experimental systems [9]. This discrepancy is due to residual TM polarized emission from the BAL arrays (which is immediately lost at the first PBS of the initial stage) and non-ideal external cavities, including slight dislocation of optical elements, undesired field reflections from their edges, or losses within them. Our simulations have shown that introducing field losses within the EC reduces the coupling efficiency, and this reduction grows linearly with the addition of new coupling stages. Therefore, one of the biggest challenges in constructing the discussed systems is minimizing field losses in the EC.

Appendix

In all formulas below, we assume that all elements of the EC are perfect, which means that the field absorption, residual reflections, and misalignments of these elements within the setup are negligible (case of $\mu = 0$ and $\kappa = 1$).

Depending on the direction of the incident beam, the transmission of the ideal PBS is given by simple projectors

$$\mathbf{M}_0^{\mathrm{bs}} = \begin{pmatrix} 1 & 0 \\ 0 & 0 \end{pmatrix}, \quad \text{or} \quad \mathbf{M}_1^{\mathrm{bs}} = \begin{pmatrix} 0 & 0 \\ 0 & 1 \end{pmatrix}.$$

The propagator $\mathbf{M}_L^{\mathrm{bc}}$ through the BC of length L exploits different group and refractive indices along the ordinary and extraordinary axes of the BC [9] and is defined as

$$\mathbf{M}_L^{\mathrm{bc}} = \tfrac{1}{2} \sum_{\iota=0}^{1} \begin{pmatrix} \zeta_0^\iota & \zeta_1^\iota \\ \zeta_1^\iota & \zeta_0^\iota \end{pmatrix} e^{ik_0(d_\iota - \nu_\iota)} M_{d_\iota}^{\mathrm{pr}} M_{\rho_\iota}^{\mathrm{sh}}, \quad \zeta_j^\iota = (-1)^{\iota j},$$

with d_ι, ν_ι, and ρ_ι defined in Eq. (5). The vector field propagation through α of $(\lambda/2^m)$-WPs is governed by the propagator $\mathbf{M}^{\mathrm{bc}}$ applied to the BC of length $\alpha\lambda_0/(2^m\Delta')$. After neglecting small, short-range angular dispersion and time delays, the corresonding operator reads as

$$\mathbf{M}_{m-1}^{\mathrm{wp}\,\alpha} \approx e^{-i\frac{2\pi n_0' \alpha}{2^m \Delta'}} \left[\tfrac{1}{2} \sum_{\iota=0}^{1} e^{i\frac{2\pi\iota\alpha}{2^m}} \begin{pmatrix} \zeta_0^\iota & \zeta_1^\iota \\ \zeta_1^\iota & \zeta_0^\iota \end{pmatrix} \right].$$

For $\alpha = 2^{m-1}$, corresponding to the $(\lambda/2)$-WP case, this operator is a simple off-diagonal matrix that exchanges the x- and y- polarized field components. Further scalar operators explored in Section 3

and Eq. (4) are defined by

$$M_d^{\rm pr}A(x)=\sqrt{\tfrac{i}{\lambda_0 d}}\int_{\mathbb{R}}e^{-ik_0[d+\frac{(x'-x)^2}{2d}]}M_{d/c_0}^{\rm sh}A(x')dx',$$
$$M^{\rm sw}A(x)=A(-x),\quad M_\tau^{\rm sh}A(t)=A(t-\tau),$$
$$A(z+0,x)=M_f^{\rm ln}A(z-0,x),\quad M_f^{\rm ln}(x)=e^{i[\phi_{\rm ln}+\frac{k_0x^2}{2f}]}.$$

The commutation of certain operators allows for the exchange of the sequence of some optical elements and the air gaps in our modeling. This results in "concentrated" air gaps of width f between the front facet of BAL$_j$ and the corresponding lens, and of width l_j-f between the lens of each BAL$_j$ and the nearest PBS [9]. The lengths of the WPs, PBSs, and lenses are ignored but can be compensated by increasing l_j.

On the way from BAL$_j$ to the OCM, the vector-field passes through the SAC lens, the (cumulative) air gap, m triples of optical elements (comprising $\alpha^s_{\lfloor j\rfloor_s}$ of $(\lambda/2^m)$-WPs, PBS, and BC) within each s-th stage of the EC, and, finally another PBS just before the OCM. The propagator of the s-th stage, $\mathbf{M}_{j,s}^{\rm cs}=\mathbf{M}_{L_s}^{\rm bc}\mathbf{M}_{j_s}^{\rm bs}\mathbf{M}_{m-1}^{{\rm wp}\,\alpha^s_{\lfloor j\rfloor_s}}$, reads as

$$\mathbf{M}_{j,s}^{\rm cs}=\tfrac{1}{4}\sum_{l''_s,l'_s=0}^{1}\eta_{j,s}^{l''_s,l'_s}\begin{pmatrix}1 & \zeta_1^{l''_s}\\ \zeta_1^{l'_s} & \zeta_1^{l'_s}\zeta_1^{l''_s}\end{pmatrix}M_{d_{l'_s}}^{\rm pr}M_{\rho_{l'_s}}^{\rm sh},$$
$$\eta_{j,s}^{l''_s,l'_s}=e^{i\frac{2\pi}{2^m}\alpha^s_{\lfloor j\rfloor_s}(l''_s-\frac{n'_0}{\Delta'})}e^{ik_0(d_{l'_s}-\nu_{l'_s})}\zeta_{j_s}^{l''_s}\zeta_{j_s}^{l'_s}.$$

Using the initial assumption $\alpha_j^0=2^{m-1}j_0$ and the binary forms of indices l' and j, we derive the single-pass propagators through all stages of the EC, $\mathbf{M}_j^{\rm acs}=\mathbf{M}_{j,m-1}^{\rm cs}\ldots\mathbf{M}_{j,1}^{\rm cs}\mathbf{M}_{j,0}^{\rm cs}$, the overall EC propagator from BAL$_j$ to the OCM, $\mathbf{M}_j^{\rm ec}$, and, finally, the beam combining operator $\mathbf{M}_{[j]}$:

$$\mathbf{M}_j^{\rm acs}=\tfrac{1}{2^m}\textstyle\sum_{l'=0}^{2^m-1}\eta_j^{l'}\begin{pmatrix}1 & 0\\ \zeta_1^{l'_{m-1}} & 0\end{pmatrix}M_{d_{l'}}^{\rm pr}M_{\rho_{l'}}^{\rm sh},$$
$$\mathbf{M}_j^{\rm ec}=\mathbf{M}_0^{\rm bs}\mathbf{M}_j^{\rm acs}M_{l_j-f}^{\rm pr}M_f^{\rm ln}M_f^{\rm pr}=\mathbf{M}_0^{\rm bs}M_j^{\rm ec},$$
$$M_j^{\rm ec}=\tfrac{1}{2^m}\textstyle\sum_{l'=0}^{2^m-1}\eta_j^{l'}M_{d_{l'}+l_j-f}^{\rm pr}M_f^{\rm ln}M_f^{\rm pr}M_{\rho_{l'}}^{\rm sh},$$
$$\mathbf{M}_{[j]}=\mathbf{M}_0^{\rm bs}\left[\sqrt{T_e}M_f^{\rm pr}M_f^{\rm ln}M_j^{\rm ec}\right]=\mathbf{M}_0^{\rm bs}M_{[j]}.$$

The beam transmission over the s-th stage in the reverse direction (from the OCM to BALs) is governed by the transposed matrices $(\mathbf{M}_{j,s}^{\rm cs})^T$. Consequently, the back-propagation through all stages of the EC and through the whole EC is defined by $(\mathbf{M}_j^{\rm acs})^T$ and $(\mathbf{M}_j^{\rm ec})^T$, respectively. Thus, the feedback operator $\mathbf{M}_{[j,r]}$ can be written as

$$\mathbf{M}_{[j,r]}=(\mathbf{M}_j^{\rm ec})^T\sqrt{R_e}\,\mathbf{M}_r^{\rm ec}=\mathbf{M}_0^{\rm bs}M_{[j,r]},$$

with an explicit definition of $M_{[j,r]}$ given in Eq. (6).

Acknowledgment

This work was inspired by the EUROSTARS Project E!10524 HIP-Lasers.

References

[1] M.S. Zediker and E.P. Zucker, “High-power diode laser technology XX: a retrospective on 20 years of progress,” *Proc. SPIE*, vol. **11983**, 1198302, 2022. doi: 10.1117/12.2615260

[2] M. Dogan, R.H. Chin, S. Fulghum, J.H. Jacob, and A.K. Chin, “Efficient pump module coupling > 1kW from a compact detachable fiber,” *Proc. SPIE*, vol. **10514**, 105140K, 2018. doi: 10.1117/12.2288468

[3] T.Y. Fan, “Laser beam combining for high-power, high-radiance sources,” *IEEE J. Sel. Top. Quantum Electron.* **11**(3), 567–577, 2005. doi: 10.1109/JSTQE.2005.850241

[4] V. Raab and C. Raab, “Mehrstufige Polarisationskopplung,” *Zeitschrift Photonik*, **5**(5), 46–49, 2004.

[5] G. Garre-Werner, J. Montiel-Ponsoda, V. Raab, G. Safont, C. Bree, M. Radziunas, C. Cojocaru, and K. Staliunas, “1 kW CW Fiber-coupled Diode Laser with Enhanced Brightness,” *Proc. SPIE*, vol. **11262**, 1126202, 2020. doi: 10.1117/12.2546086

[6] H. Wenzel, “Basic aspects of high-power semiconductor laser simulation,” *IEEE J. of Selected Topics in Quantum Electronics*, **19**(5), 1502913, 2013. doi: 10.1109/JSTQE.2013.2246774

[7] A. Zeghuzi, M. Radziunas, H.-J. Wünsche, J.-P. Koester, H. Wenzel, U. Bandelow, and A. Knigge, “Traveling wave analysis of non-thermal far-field blooming in high-power broad-area lasers,” *IEEE J. of Quantum Electronics*, **55**(2), 2000207, 2019. doi: 10.1109/JQE.2019.2893352

[8] A. Zeghuzi, H.-J. Wünsche, H. Wenzel, M. Radziunas, J. Fuhrmann, A. Klehr, U. Bandelow, and A. Knigge, “Time-dependent simulation of thermal lensing in high-power broad-area semiconductor lasers,” *IEEE J. of Selected Topics in Quantum Electronics* **25**(6), 1502310, 2019. doi: 10.1109/JSTQE.2019.2925926

[9] C. Bree, V. Raab, J. Montiel-Ponsoda, G. Garre-Werner, K. Staliunas, U. Bandelow, and M. Radziunas, “Beam-combining scheme of high-power broad-area semiconductor lasers with Lyot-filtered reinjection: modeling, simulations, and experiments,” *J. Opt. Soc. Am. B*, **36**(7), 1721–1730, 2019. doi: 10.1364/JOSAB.36.001721

[10] “BALaser: a software tool for simulation of dynamics in Broad Area semiconductor Lasers,” `http://www.wias-berlin.de/software/balaser`.

[11] J. E. Boschker, U. Spengler, P. Ressel, M. Schmidbauer, A. Mogilatenko, and A. Knigge, “Stability of ZnSe-Passivated Laser Facets Cleaved in Air and in Ultra-High Vacuum,” *IEEE Photonics Journal*, vol. 14, 1531606, 2022, doi: 10.1109/JPHOT.2022.3176675